

1 **Side Area-Assisted 3D Evaporator with Antibiofouling Function for Ultra-Efficient Solar**  
2 **Steam Generation**

3  
4  
5 Haoxuan Li,<sup>1,2,3,4†</sup> Wei Zhu,<sup>1,2,4†</sup> Meng Li,<sup>1,2,4</sup> Ying Li,<sup>1\*</sup> Ryan T. K. Kwok,<sup>4</sup> Jacky W. Y. Lam,<sup>4</sup>  
6 Lei Wang,<sup>1,2</sup> Dong Wang,<sup>1\*</sup> Ben Zhong Tang<sup>4\*</sup>  
7  
8

9 **Affiliations**

10 1 Centre for AIE Research, Shenzhen Key Laboratory of Polymer Science and Technology,  
11 Guangdong Research Center for Interfacial Engineering of Functional Materials, College of  
12 Material Science and Engineering, Shenzhen University, Shenzhen 518061, P. R. China

13 2 Key Laboratory of Optoelectronic Devices and Systems of Ministry of Education and  
14 Guangdong Province, College of Physics and Optoelectronic Engineering, Shenzhen University,  
15 Shenzhen 518061, P. R. China

16 3 Key Laboratory of Eco-Textiles (Ministry of Education), Nonwoven Technology Laboratory,  
17 Jiangnan University, Wuxi 214122, China

18 4 Department of Chemistry, The Hong Kong University of Science and Technology, Clear Water  
19 Bay, Kowloon, Hong Kong, China

20 †These authors contributed equally to this work

21 \*Corresponding author. Email: wangd@szu.edu.cn, liyingway@szu.edu.cn, tangbenz@ust.hk  
22

23 **Teaser**

24 We report a porous all-fiber porous cylinder like foam (AFPCF) containing AIE luminogen  
25 (AIEgens) with superior capacities of photothermal conversion and ROS generation to  
26 simultaneously realize efficiently solar steam generation and antibiofouling effects.  
27

28 **Abstract**

29 Solar-driven interfacial steam generation (SISG) has been recognized as the most promising  
30 strategy to solve water shortages in an eco-friendly and low-cost way. However, the practical  
31 application of SISG is vitally restricted by some inherent limits, especially for finite evaporation  
32 rate and insufficient working life of evaporator. Herein, we explore a novel SISG system  
33 involving an all-fiber porous cylinder-like foam (AFPCF) 3D evaporator, side area-assisted  
34 evaporation protocol, and aggregation-induced emission (AIE)-active molecules with “one stone  
35 two birds” function. The AIE-featured solar absorber exhibits highly efficient sunlight absorption  
36 and photothermal conversion, endowing the side area-assisted evaporator with as high as 3.6 kg

37  $\text{m}^{-2} \text{h}^{-1}$  of solar evaporation rate under 1 sun of irradiation. Moreover, the evaporator is capable of  
38 powerfully producing reactive oxygen species (ROS) upon sunlight irradiation benefiting the  
39 prominent photosensitizing property of the AIE molecules, which results in extraordinary  
40 photodynamic killing of bacteria nearby the fiber to prevent biofouling, consequently improving  
41 the working life of evaporator.

42  
43  
44  
45

## 46 **Introduction**

47 Solar driven interfacial steam generation (SISG) is a desirable strategy to continuously produce  
48 clean water by utilizing sea water and solar energy, which both are considered as inexhaustible  
49 recourses on the earth. (1-3) Of particular importance, SISG is indeed a zero-carbon emission  
50 process, making it a great potential candidate to alleviate the global water scarcity. (4, 5) Over the  
51 past decades, enthusiastic efforts have been devoted by scientists on designing ideal evaporator,  
52 comprised of solar absorber for efficient light-to-heat conversion as well as floating structure for  
53 thermal insulation and water transportation, to increase the evaporation rate. (6-8) Compared to  
54 two-dimensional (2D) evaporator, three-dimensional (3D) analogues exhibit excellent evaporation  
55 performance due to the reduced light reflection and gaining energy from the environment. (9,10)  
56 For example, by increasing the height of the cylindrical cup-shaped structure, the evaporator can  
57 generate vapor with an evaporation rate of  $2.04 \text{ kg m}^{-2} \text{ h}^{-1}$  under the irradiation of 1 sun, far  
58 exceeding that for 2D structure ( $1.21 \text{ kg m}^{-2} \text{ h}^{-1}$ ). (11) Another typical 3D cone structure can  
59 achieve an evaporation rate of  $1.7 \text{ kg m}^{-2} \text{ h}^{-1}$ , 1.7 times higher than that of planar film. (12)  
60 However, nearly all of the previous works set the irradiation of simulated sun in vertical direction  
61 during evaporation test, while the irradiation in tilt direction had been rarely investigated.  
62 Inspired by that, side area-assisted evaporation attracted our attention for designing 3D evaporator,  
63 wherein both surface area and side area of the evaporator can absorb solar energy under natural  
64 sunlight due to its tilt irradiation function, which could consequentially amplify both effective  
65 heating area and evaporation rate. Hence, side area-assisted evaporation may offer a feasible and  
66 simple protocol to design advanced evaporator to beyond the limitation of evaporation efficiency.

67 The solar absorber can be categorized as plasmonic materials, carbon-based materials and  
68 organic molecules. (13-18) Among them, plasmonic and carbon-based absorbers have their  
69 inherent weaknesses, such as low chemical stability and high cost for plasmonic absorbers, and  
70 low stability against water and bacteria for carbon absorbers. (19-21) Besides, those developed

---

71 systems generally feature a single function with transferring solar energy into heat, and  
72 multifunctional evaporator remain unexploited but supremely desirable. Especially, during  
73 evaporation, the formed warm environment around the evaporator is capable of promoting the  
74 growth of microorganisms which seriously affects working life of the evaporator. Therefore,  
75 exploiting functional absorber to simultaneously achieve efficient evaporation and antibiofouling  
76 property is a major requirement. (22, 23) In conventional methods, Ag, (20) ZnO (21)  
77 nanoparticles and Mxene (24) are additionally doped into evaporator as bacteriostatic agent,  
78 endowing the evaporator with antibiofouling behavior to prevent channel plugging caused by  
79 microorganisms proliferation. Those strategies, however, require tedious labor in the preparation  
80 process and influence evaporation output due to the insufficient compatibility. Evidently, the  
81 exploration of a single material sharing both photothermal conversion and antibiofouling  
82 capacities would be an appealing yet significantly challenging task. In the circumstances, as a  
83 newly emerged photosensitizing agent, aggregation-induced emission (AIE)-active molecule that  
84 could simultaneously afford high performance photothermal conversion and reactive oxygen  
85 species (ROS) production through rational design, (25-28) could be an ideal candidate for  
86 constructing 3D evaporator with efficient evaporation and antibiofouling functions.

87 In this work, we report a porous all-fiber porous cylinder like foam (AFPCF) containing AIE  
88 luminogen (AIEgens) with superior capacities of photothermal conversion and ROS generation to  
89 simultaneously realize efficiently solar steam generation and antibiofouling effects (Fig.1A). Side  
90 area-assisted evaporation and antibiofouling activity is for the first time integrated into an  
91 evaporator. This presented evaporator features an interconnected porous structure with excellent  
92 hydrophilicity for vapor escaping and water supplying, side-area assisted evaporation system for  
93 increased effective evaporation area, as well as efficient photodynamic killing of bacteria nearby  
94 the fiber to prevent biofouling, collectively offering a design blueprint for the next generation of  
95 solar steam production materials.

## 96 **Results and Discussion**

### 97 **Fabrication and characterization of AFPCF**

98 As shown in Fig. 1A, a typical D-A-D molecule (TPA-BTDH) were well designed and facilely  
99 synthesized in three steps (Fig. S1). In the primary step, Suzuki-Miyaura coupling reaction  
100 smoothly proceeded by employing 4-methoxy-N-(4-methoxyphenyl)-N-(4-(4,4,5,5-tetramethyl-  
101 1,3,2-dioxaborolan-2-yl)phenyl)aniline and 4,7-dibromo-5,6-dinitrobenzo[c][1,2,5]thiadiazole as  
102 starting materials, producing TPA-BTDNO with a yield of 53.2%. Iron-catalyzed nitro reduction  
103 of TPA-BTDNO was next conducted in the presence of acetic acid and iron powder, yielding  
104 intermediate product TPA-BTDNH. Subsequent cyclization with benzils to obtain the TPA-

---

105 BTDH with a yield of 95.6%. The intermediates and final compounds are characterized by <sup>1</sup>H  
106 NMR, <sup>13</sup>C NMR, and high-resolution mass spectrum (HRMS). The single crystal of TPA-BTDH  
107 was obtained in chloroform/hexane under slow evaporation. As shown in Fig. 1B and Table. S1,  
108 the intermolecular distances between two parallel planes were as large as 3.609 Å and 6.702 Å  
109 respectively, which exceeding the typical  $\pi$ - $\pi$  stacking that usually quenches the fluorescence.  
110 The twisted angles between the acceptor TQ and donor MTPA of TPA-BTDH were 51.8°, and the  
111 other dihedral angles inside the molecule were 69.71° and 72.4°, and 58.81°, respectively (Fig.  
112 S2A). All these features of TPA-BTDH including abundant molecular rotators, large twisted  
113 angles and the nonplanar structure, may enable its intramolecular motions to be partially restricted  
114 but still active in fiber state, potentially allowing high photothermal conversion and ROS  
115 generation benefiting from the balanced energy dissipations (Fig. 1C).

116 As illustrated in Fig. 1D, the maximum absorption wavelength of TPA-BTDH was located at  
117 645 nm and the photoluminescence (PL) spectra of TPA-BTDH were peaked at 908 nm in the  
118 NIR-II region. The strong and broad absorption is beneficial to absorbing the light energy of  
119 sunlight. In addition, the long-wavelength absorption was determined to be in good accordance  
120 with the narrow HOMO-LUMO bandgap of (1.702 eV) (Fig. S2B). Subsequently, the  
121 photosensitizing properties of TPA-BTDH were investigated in terms of ROS production and  
122 photothermal conversion. It was observed that the emission intensity of ROS indicator DCFH-DA  
123 was remarkably boosted with a 195-fold enhancement, revealing the high efficiency of ROS  
124 generation (Fig. 1E). Upon solar irradiation of 1 sun, the temperature of TPA-BTDH powder  
125 increased with time and reached a maximum of 62.8 °C within 150 s, suggesting its excellent  
126 capacity of transferring solar energy to heat (Fig. 1F).

127 Encouraged by the excellent properties of TPA-BTDH, 3D-architecture nanofibrous mat with  
128 TPA-BTDH as solar absorber was then fabricated by using gas-forming technology. (17,29)  
129 Firstly, TPA-BTDH were doped into fiber during electrospinning. The absorber would be stable  
130 given that TPA-BTDH was wrapped in the polymethyl methacrylate (PMMA) rather than coating  
131 on the matrix surface (Fig. S3A and S3B). Even though their absorption was limited in the range  
132 from 550 to 1000 nm (Fig. S3C), the TPA-BTDH/PMMA nanofibrous mat had over 80% of light  
133 absorption and showed considerable capacity for transferring solar to heat. The temperature of the  
134 mat could increase to 61.5 °C under 150 s of 1 sun irradiation (Fig. S3D). Subsequently, the TPA-  
135 BTDH/PMMA nanofibrous mats were cut into a circle with the diameter of 3 cm, treated by  
136 plasma for improving their hydrophilic, and then expanded in the NaHB<sub>4</sub> solution (1M) for  
137 different time (Fig. 2A). With the gas bubble generated and escaped through the mats (Fig. 2B),  
138 thickness changes of the nanofibrous mat following expansion were shown in Fig. 2C. Evidently,

---

139 the height of expanded 3D AFPCF increased from 1 to 3 and 5 cm, as the expansion time  
140 increased from 10 to 30 and 60 min, respectively. To be noted that, the hydrophilicity of the 2D  
141 nanofibrous mats given by plasma treatment is the key factor for expanding into 3D structure.  
142 Aiming to investigate the relationship between side area and evaporation rate, we prepared three  
143 groups 3D AFPCF with the height of 1, 3 and 5 cm, and the corresponding effective areas were  
144 about 10, 16 and 22 cm<sup>2</sup>, respectively (Fig. 2D). The scanning electron microscope (SEM) images  
145 revealed that gap between each layer of nanofiber was observed to increase with raising  
146 expansion time, and the thickness of layer was decreased (Fig. 2E and Fig. S4). Such all-fiber  
147 structure bearing both interconnected pore and superior hydrophilicity endowed the 3D AFPCF  
148 with water transportation and vapor escape functions. As depicted by UV-vis-NIR absorption  
149 spectrum of the 3D AFPCF in Fig. 2F, the 3D AFPCF exhibited efficient absorption in the range  
150 from 500 to 1000 nm, which is the main light energy band of natural sun, suggesting that the 3D  
151 AFPCF possesses excellent capacity to absorb sunlight. It was observed that the temperature of  
152 AFPCF in dry state rose to 59.2 °C within 10 min upon 1 sun irradiation (Fig. S5). The high  
153 localized temperature on the surface of the AFPCF is beneficial for solar steam generation. (30)

#### 154 **Side area assisted evaporation**

155 To explore its solar steam generation ability, AFPCF with the height of 3 cm was wrapped by  
156 foam and then floated on a beaker filled with 3.5 wt% NaCl solution in water (Fig. 3A). The  
157 temperatures of the evaporator surface and side areas were also recorded by IR camera to  
158 investigate the effect of the irradiation direction of the simulated sunlight on the evaporation  
159 capacity (Fig. 3B and 3C). As the irradiation direction was set as vertical to the evaporator, the  
160 temperature of evaporator surface was increased to 46.5 °C within 1 h, which was much higher  
161 than that of the evaporator side (only 28.9 °C). In addition, as the irradiation direction was tilted  
162 to the evaporator (with incident angle of 60°), the temperatures of evaporator surface and side  
163 were increased to 44.5°C and 39.5 °C within 1 h, respectively. Therefore, both surface and side of  
164 the evaporator acted as heated evaporation area to generate vapor during solar tilt irradiation. In  
165 this way, the effective evaporation area can be greatly increased without the increase of the  
166 evaporator surface. The mass of simulated seawater decreased with the increased of irradiation  
167 time (Fig. 3D). Under the vertical irradiation of 1 sun, the evaporation rate of the evaporator was  
168 determined to be 2.4 kg m<sup>-2</sup> h<sup>-1</sup>, and the corresponding dark evaporation rate was 0.8 kg m<sup>-2</sup> h<sup>-1</sup>.  
169 Notably, as the vertical irradiation was turned to the tilted irradiation, a dramatic increase in the  
170 evaporation rate from 2.4 to 3.6 kg m<sup>-2</sup> h<sup>-1</sup> was revealed mainly due to the additional heat  
171 generated by the side area, and the high evaporation rate remained stable over time (Fig. 3E).

---

172 These results indicated that side area-assisted evaporation is a facile strategy to enhance the  
173 overall evaporation based on the natural sunlight tilting irradiation.

174 To systematically investigate the effect of side area on the evaporation performance, the  
175 evaporators with height of 1 and 5 cm were also tested under the vertical and tilted irradiation of 1  
176 sun (Fig. S6). Under the vertical and tilted irradiation for 1 h, the surface temperature of the 1  
177 cm-height evaporator reached at 42.2 and 41.5 °C, respectively (Fig. S7), while its side  
178 temperature was not recorded, since the side area was not sufficient enough to absorb solar energy.  
179 In the case of 5 cm-height evaporator, upon vertical and tilted irradiation for 1 h, the surface  
180 temperatures were measured to be 43.3 and 42.5 °C, respectively, while the side temperatures  
181 were determined to be 28.2 and 36.2 °C (Fig. S6C). Moreover, the corresponding evaporation  
182 rates were calculated to be 1.6 and 1.8 kg m<sup>-2</sup> h<sup>-1</sup> for the 1 cm-height evaporator, and 2.8 and 3.2  
183 kg m<sup>-2</sup> h<sup>-1</sup> for the 5 cm-height evaporator, under the vertical and tilted irradiation of 1 sun (Fig.  
184 S6D and 6E), respectively. These results indicated that the evaporation rate can be significantly  
185 enhanced by increasing the height of the evaporator. It was also found that the evaporation rate of  
186 5 cm-height evaporator was lower than that of the 3 cm-height evaporator, which can be  
187 attributed to the restrained water transportation in the case of 5 cm-height evaporator. This issue  
188 could be solved by constructing 3D smart floating structure, which can transport water to higher  
189 altitude. According to classical energy efficiency calculations, all the evaporators with different  
190 side areas showed the evaporation rate beyond the theoretical limit of about 1.47 kg m<sup>-2</sup> h<sup>-1</sup>, which  
191 can be attributed to the additional energy harvest by the side area which absorbed the sunlight.  
192 Indeed, the presented evaporator remarkably offers a design philosophy to significantly enhance  
193 the evaporation performance.

#### 194 **Antibiofouling performance**

195 Working life is a key criterion to estimate a evaporator. As known that a warm environment  
196 around the evaporator can be formed during the evaporation process, and promote the growth of  
197 microorganisms, which seriously affects the working life of evaporator. Inspired by the efficient  
198 ROS generation of TPA-BTDH, as well as high efficiency of bacteria photodynamic killing, the  
199 antibiofouling effect of the AFPCF was assessed by attaching four typical bacteria, *Escherichia*  
200 *coli* (*E. coli*), *Staphylococcus epidermidis* (*S. epidermidis*), *Staphylococcus aureus* (*S. aureus*)  
201 and methicillin-resistant *Staphylococcus aureus* (MRSA) on the evaporator surface, respectively.  
202 For the contact-kill test, the blank control and AFPCF samples with a diameter of 1.5 cm were  
203 loaded with 100 μL PBS containing 1×10<sup>7</sup> CFU mL<sup>-1</sup> bacteria, then antibacterial assay was  
204 assessed by agar plate counting. For accuracy, six parallel samples were placed on each group. As  
205 shown in Fig. 3F, four types of bacteria grow well in the blank control plate after the radiation of

---

206 the simulated sunlight for 10 min. In contrast, within 10 min of irradiation, 99.86% *E. coli*,  
207 99.91% *S. epidermidis*, 99.96% *S. aureus* and 99.98% MRSA were killed rapidly by AFPCF,  
208 owing to its superior capability to generate ROS under visible light (Fig. S8). Moreover,  
209 considering that the AFPCF is easy to generate ROS incessantly under the sunlight, enabling the  
210 evaporator to suppress attachment and proliferation of bacteria and/or microorganisms on the  
211 nanofiber, resulting in good antibiofouling of the evaporator. We also used *E. coli* as a model to  
212 investigate the antibacterial performance of the AFPCF at alternate day and night. Each cycle  
213 includes three stages, pipetting  $1 \times 10^6$  CFU mL<sup>-1</sup> *E. coli* on the AFPCF, incubating them in dark  
214 condition for 50 min and exposing them to simulated sunlight for 10 min. Five cycles of the  
215 antibacterial result indicated that the biocidal efficacy of the AFPCF maintained constance with a  
216 99.9% inhibiting rate against *E. coli* (Fig. 3G). Moreover, it was revealed that the AFPCF cannot  
217 generate ROS at night, due to the lack of light to drive molecule excitation, revealing the weakly  
218 antibacterial capacity in dark condition (Fig. S9). This cycle test also suggested that the bacteria  
219 accumulated on the nanofiber at night can be killed at daytime, showing excellent service life  
220 with self-antibiofouling property.

221 The morphological changes of bacteria on the nanofiber with or without light irradiation were  
222 visualized by SEM. Both *E. coli* and *S. aureus* exhibited rod and spherical shape with smooth  
223 surface in the darkness. As shown in Fig. S10, the cellular destruction and surface wrinkled of the  
224 *E. coli* together with the lesions of *S. aureus* were observed on the surface of the nanofiber after  
225 the AFPCF exposure to 10 min of simulated sunlight irradiation. This observation indicated that  
226 the bacteria on the nanofiber can be easily killed via disrupting bacterial cell membranes, which is  
227 similar to peroxide disinfectants. Apart from killing the bacteria attached on the nanofiber, the  
228 AFPCF can also kill the bacteria nearby the evaporator, offering a facile strategy to clean up the  
229 polluted lake and/or river. In additon, the antibacterial activity of the AFPCF under natural  
230 sunlight irradiation was also investigated. As illustrated in Fig. S11, each well of the six-well  
231 plate was pipetted 5 mL PBS solution containing  $10^7$  CFU mL<sup>-1</sup> bacteria, and three groups of *E.*  
232 *coli*, *S. aureus* and MRSA were tested, respectively. The AFPCF was placed on three wells, and  
233 other three wells was set as blank control. Under the irradiation of natural sunlight with  $0.76$  kW  
234 m<sup>-2</sup> for 1 h (2:00 PM to 3:00 PM), viable colonies of *E. coli*, *S. aureus* and MRSA grew well on  
235 the plates in the absence of AFPCF, whereas a significant decrease in all types of bacteria survival  
236 occurred in the presence of AFPCF, which should be attributed to the ROS generation. Owing to  
237 excellent insulation performance of the AFPCF, there is no significant changes in temperature of  
238 PBS solution with or without AFPCF under the irradiation of sunlight. Hence, ROS played a key  
239 role in killing bacteria. Limited by the operating distance of ROS, only the bacteria near the

---

240 evaporator can be efficiently killed, which is beneficial to treat surface water pollution without  
241 affecting on fish or other organisms living in deep water.

### 242 **Solar water purification based on the AFPCF**

243 To explore the water purification capacity of the AFPCF, two samples including simulated  
244 seawater containing five primary ions ( $\text{Na}^+$ ,  $\text{Mg}^{2+}$ ,  $\text{K}^+$ ,  $\text{Ca}^{2+}$  and  $\text{Pb}^{2+}$ ) and waste water containing  
245 four types of bacteria (*E. coli*, *S. epidermidis*, *S. aureus*, MRSA) were carefully prepared. In order  
246 to collect purified water from the samples, we also hand-made a closed evaporation system,  
247 which consists of a glass cover with high transmittance, a Dewar Flask filled with sample water  
248 and the evaporator (Fig. 4A). We first used the simulated seawater to conduct the test, as the  
249 evaporation system under the tilted irradiation of 1 sun, vapor generated and condensed on the  
250 inner wall of the glass cover (Fig. S12). With the increase of the irradiation time, the vapor  
251 became liquid and formed droplets which merged together (Fig. 4B). After purification by the  
252 solar driven evaporation system, the light yellow-colored simulated seawater was transferred into  
253 a colorless and clear liquid (Fig. S13). As noted by inductively coupled plasma mass spectrometry  
254 (ICP-MS), the concentration of ions ( $\text{Na}^+$ ,  $\text{Mg}^{2+}$ ,  $\text{K}^+$ ,  $\text{Ca}^{2+}$  and  $\text{Pb}^{2+}$ ) in the simulated seawater  
255 decreased from  $10^3$  to  $10^{-1}$   $\text{mg L}^{-1}$  with an efficiency of 99.9% after solar evaporation treatment,  
256 which was much lower than the World Health Organization (WHO) standard for drinking water  
257 (1‰) (Fig. 4C). (31) Apart from ions pollutants, bacteria and microorganism pollution is another  
258 challenge for water purification. We then utilized the evaporation system to purify the waste  
259 water containing four types of bacteria. As shown in Fig. 4D and 4E, there is no any bacterial  
260 clone could be observed in the condensed water, showing the efficient removal of the bacteria.  
261 These results strongly suggested that this developed AFPCF evaporator was capable of achieving  
262 water purification from seawater and waste water via solar irradiation.

### 264 **Conclusion**

265 In summary, an advanced 3D evaporator, namely AFPCF, that combines side area-assisted  
266 evaporation with a “One Stone Two Birds” AIEgen is developed to realize excellent evaporation  
267 property and antibiofouling performance. AFPCF evaporator exhibits interconnected pore and  
268 large side area, which are beneficial for vapor escaping and gaining energy from tilted sunlight  
269 irradiation. The presence of the tactfully designed AIEgen endows the evaporator with excellent  
270 photothermal conversion and photodynamic antibacterial capacity. Notably, solar evaporation rate  
271 of the evaporator is determined to be as high as  $3.6 \text{ kg m}^{-2} \text{ h}^{-1}$ , which is far beyond the theoretical  
272 limit ( $1.62 \text{ kg m}^{-2} \text{ h}^{-1}$ ) under 1 sun of irradiation. Moreover, the continuous ROS generation of  
273 the AIEgen under the irradiation of sunlight highly inhibits the growth of bacteria nearby the

---



274 evaporator, revealing the superior antibiofouling performance. The presented evaporator is further  
275 used to purify simulated seawater and waste water containing various bacteria, and achieved a  
276 high quality purification meeting the WHO standards for drinking water. Therefore, the  
277 multifunctional side area-assisted evaporator opened a window to construct next generation of  
278 smart evaporator for water purification and other applications, including moisture management,  
279 Marine ecosystem, and sewage treatment.

## 281 **Materials and Methods**

282 **Chemicals and materials:** Poly(methyl methacrylate) (PMMA) ( $M_w = 120\,000$ ), tetrahydrofuran  
283 (THF), N, N-dimethylformamide (DMF), and sodium borohydride were all obtained from Merck  
284 (Darmstadt, Germany). 4,7-dibromobenzo[c][1,2,5]thiadiazole, benzil, Pd(PPh<sub>3</sub>)<sub>4</sub>, 4-methoxy-N-  
285 (4-methoxyphenyl) -N-(4-(4,4,5,5-tetramethyl-1,3,2-dioxaborolan-2-yl)phenyl)aniline were  
286 purchased from Bidepharm (Shanghai, China). All the chemicals used as received without further  
287 purification. Luria-Bertani (LB) broth and LB agar were from USB Co. Zinc dust. Phosphate  
288 buffer saline (PBS) was from Sigma-Aldrich. E. coli (ATCC 25922), S. epidermidis (ATCC) and  
289 S. aureus (ATCC) were from ATCC. MRSA were from Beijing Tiantan Hospital (China), Milli-Q  
290 water was from a Milli-Q purification system (Merck Millipore, Germany).

291 **Preparation of TPA-BTDH/PMMA nanofibrous mat:** For electrospun TPA-BTDH/PMMA  
292 nanofibers, the solution for electrospinning was prepared by dissolving 1.0 g of PMMA in 10 mL  
293 mixture of THF and DMF (v/v = 7:3) at a final concentration of 10 wt.%, and then 50 mg of TPA-  
294 BTDH powders were added into the as-prepared solution. The solution was loaded into a 5-mL  
295 plastic syringe with a 21-gauge needle attached and dispensed using a KD Scientific syringe  
296 pump. The injection rate was set at 1 mL/h. A voltage of 13 kV generated by Gamma High  
297 Voltage was applied to the needle, while the distance between the tip of the needle to the collector  
298 was set to 15 cm, electrospun time was set to 12 h.

299 **Fabrication of AFPCF:** TPA-BTDH/PMMA nanofibrous mats were cut into a circle with the  
300 diameter of 3 cm, and then treated by plasma for 5 min to improve their hydrophilicity. During  
301 expansion, the prepared nanofibrous mats were immersed in 100 mL NaBH<sub>4</sub> solution (1 M) for  
302 varying of time (0, 10, 30 and 60 min) at room temperature. Following expansion, the NaBH<sub>4</sub>  
303 solution was discarded and the expanded TPA-BTDH/PMMA nanofiber foam were gently  
304 transferred into a beaker and rinsed three times with deionized water to remove sodium salt.

305 **Characterization:** The SEM images of samples were observed using a FEI APREOS field  
306 emission scanning electron microscopy (FE-SEM) (Thermal, Japan). The IR thermal images and  
307 digital photographs were taken by E6 IR-camera (FLIR, USA) and mate-20 pro mobile phone

---

(HUAWEI, China), respectively. <sup>1</sup>H spectra were measured on Bruker AVANCE III 600M NMR spectrometers. Absorbance spectra were recorded using PerkinElmer Lambda 950 (PERKINELMER, USA). The concentration of ions was tracked by ICP-OES (ICAP 7000, USA) with dilutions in 2% HNO<sub>3</sub> to make the loaded ion concentration lower than 10 parts per million.

**Solar steam generation measurements:** The experiment of photothermal properties was performed by a Solar-500L solar simulator system (NBET, Beijing), which contains a solar simulator and an AM 1.5G light filter. The solar density is calculated by a VLP-2000 light power meter (LASER, China). The temperature changes of the samples were taken by E6 IR-camera (FLIR, USA). For tilted irradiation test, the irradiation direction was set as tilted to the evaporator with incident angle of 60°, to ensure that the surface and side area of AFPCF can be fully irradiated. The mass change of water was measured via a PR224ZH high accuracy balance (OHAUS, New Jersey).

**Antibacterial Activity Assay:** AFPCF samples were cut into 1.0 cm in diameter and placed in a 48-well plate. The samples were challenged with *E. coli*, *S. epidermidis*, *S. aureus* and MRSA bacteria at a concentration of 1 × 10<sup>6</sup> CFU mL<sup>-1</sup>. 1 × 10<sup>7</sup> CFU mL<sup>-1</sup> bacteria were dispersed in 1 mL PBS solution. 100 μL of the bacteria solution was added into 48-well plate. *E. coli*, *S. epidermidis*, *S. aureus* and MRSA after being treated with or without AFPCF-3cm under dark condition and simulated sunlight irradiation for 10 min after static 10 min. Last, 50 μL bacteria solution spread onto a LB agar plate and incubated at 37 °C for 24 h. Colonies were counted and colony forming unit (CFU mL<sup>-1</sup>) were calculated. Experiments were performed with three replicates.

AFPCF samples were cut into 3.0 cm in diameter and placed in a 6-well plate. The samples were challenged with *E. coli*, *S. aureus* and MRSA bacteria at a concentration of 1 × 10<sup>8</sup> CFU mL<sup>-1</sup>. 100 μL of the bacteria solution was added into 6-well plate and then 4 mL PBS was added to prevent water loss from the sunlight. 100 μL bacteria solution was spread onto a LB agar plate and incubated at 37 °C for 24 h after nature sun irradiation for 60 min. Colonies were counted and CFU mL<sup>-1</sup> were calculated. Experiments were performed with three replicates.

## References

1. P. Tao, G. Ni, C. Song, W. Shang, J. Wu, J. Zhu, G. Chen, T. Deng, Solar-driven interfacial evaporation. *Nat. Energy* 3, 1031-3041 (2018).
-

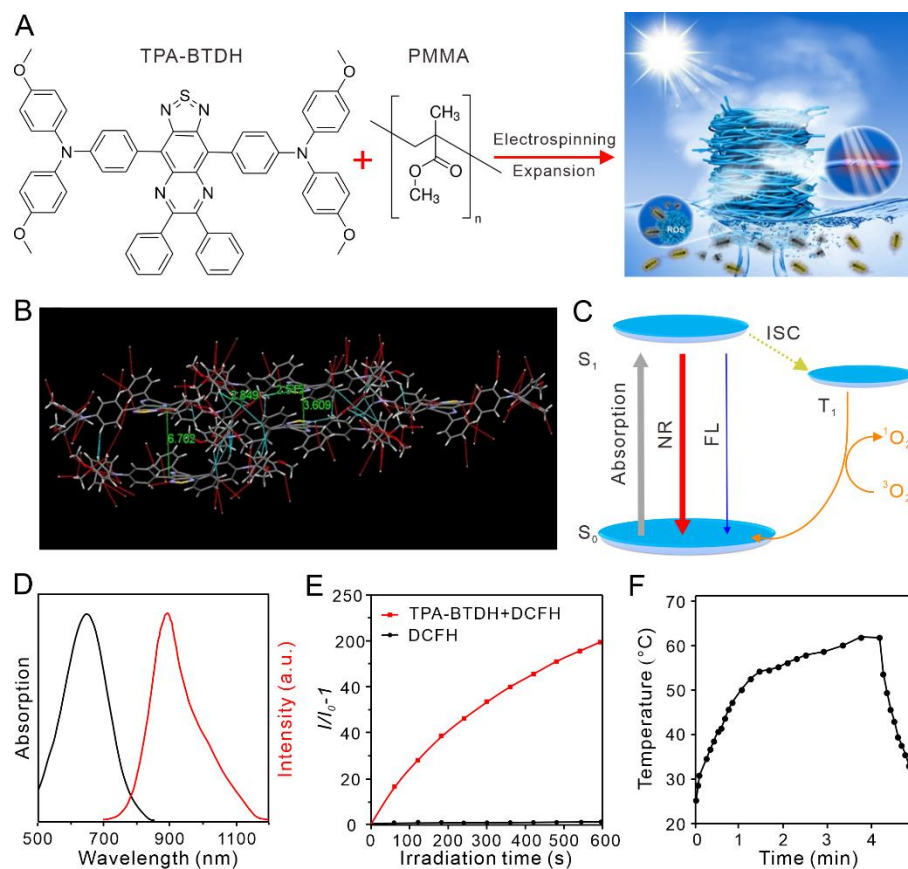
- 342 2. F. Zhao, Y. Guo, X. Zhou, W. Shi, G. Yu, Materials for solar-powered water evaporation. *Nat.*  
343 *Rev. Mater.* 5, 388-401 (2020).
- 344 3. M. Gao, L. Zhu, C. K. Peh, G. W. Ho, Solar absorber material and system designs for  
345 photothermal water vaporization towards clean water and energy production. *Energy Environ.*  
346 *Sci.* 12, 841-864 (2019).
- 347 4. L. Zhou, X. Li, G. W. Ni, S. Zhu, J. Zhu, The revival of thermal utilization from the Sun:  
348 interfacial solar vapor generation. *Natl. Sci. Rev.* 6, 562-578 (2019).
- 349 5. Y. Guo, H. Lu, F. Zhao, X. Zhou, W. Shi, G. Yu, Biomass-derived hybrid hydrogel  
350 evaporators for cost-effective solar water purification. *Adv. Mater.* 32, 1907061 (2020).
- 351 6. Y. Pang, J. Zhang, R. Ma, Z. Qu, W. Lee, T. Luo, Solar-thermal water evaporation: a review.  
352 *ACS. Energy Lett.* 5, 437-456 (2020).
- 353 7. J. Zhou, Y. Gu, P. Liu, P. Wang, L. Miao, J. Liu, A. Wei, X. Mu, J. Li, J. Zhu, Development  
354 and evolution of the system structure for highly efficient solar steam generation from zero to  
355 three dimensions. *Adv. Funct. Mater.* 50, 1903255 (2019).
- 356 8. Y. S. Jun, X. Wu, D. Ghim, Q. Jiang, S. Cao, S. Singamaneni, Photothermal membrane water  
357 treatment for two worlds. *Acc. Chem. Res.* 52, 1215-1225 (2019).
- 358 9. N. Xu, X. Hu, W. Wu, X. Li, L. Zhou, S. Zhu, J. Zhu, Mushrooms as efficient solar steam-  
359 generation devices. *Adv. Mater.* 29, 1606762 (2017).
- 360 10. Y. Wang, X. Xu, B. Shao, X. Yang, G. Owens, H. Xu, Boosting solar steam generation by  
361 structure enhanced energy management. *Sci. Bull.* 65, 1380-1388 (2020).
- 362 11. Y. Shi, R. Li, Y. Jin, S. Zhuo, L. Shi, J. Chang, S. Hong, K. C. Ng, P. Wang, A 3D  
363 photothermal structure toward improved energy efficiency in solar steam generation. *Joule* 2,  
364 1171-1186 (2018).
- 365 12. Y. Wang, C. Wang, X. Song, M. Huang, S. K. Megarajan, S. F. Shaikat, H. Jiang, Improved  
366 light-harvesting and thermal management for efficient solar-driven water evaporation using  
367 3D photothermal cones. *J. Mater. Chem. A* 6, 9874-9881 (2018).
- 368 13. X. Zhou, F. Zhao, Y. Guo, B. Rosenberger, G. Yu, Architecting highly hydratable polymer  
369 networks to tune the water state for solar water purification. *Sci. Adv.* 5, eaaw5484 (2019).
- 370 14. N. Xu, J. Li, Y. Wang, C. Fang, X. Li, Y. Wang, L. Zhou, B. Zhu, Z. Wu, S. Zhu, J. Zhu, A  
371 water lily-inspired hierarchical design for stable and efficient solar evaporation of high-  
372 salinity brine. *Sci. Adv.* 5, eaaw7013 (2019)
- 373 15. L. Zhou, Y. Tan, J. Wang, W. Xu, Y. Yuan, W. Cai, S. Zhu, J. Zhu, 3D self-assembly of  
374 aluminium nanoparticles for plasmon-enhanced solar desalination. *Nat. Photon.* 10, 393-398  
375 (2016).
-

- 376 16. Y. Kuang, C. Chen, S. He, E. M. Hitz, Y. Wang, W. Gan, R. Mi, L. Hu, A high-performance  
377 self-regenerating solar evaporator for continuous water desalination. *Adv. Mater.* 31,  
378 1900498 (2019).
- 379 17. H. Li, H. Wen, Z. Zhang, N. Song, R. T.K. Kowk, J. W. Y. Lam, L. Wang, D. Wang, B. Z.  
380 Tang, Reverse thinking of the aggregation-induced emission principle: amplifying molecular  
381 motions to boost photothermal efficiency of nanofibers. *Angew. Chem. Int. Ed.* 59, 20371-  
382 20375 (2020).
- 383 18. H. Li, H. Wen, J. Li, J. Huang, D. Wang, B. Z. Tang, Doping AIE photothermal molecule into  
384 all-fiber aerogel with self- pumping water function for efficiency solar steam generation. *ACS*  
385 *Appl. Mater. Interfaces* 12, 26033-26040 (2020).
- 386 19. C. Liu, K. Hong, X. Sun, A. Natan, P. Luan, Y. Yang, H. Zhu, An ‘antifouling’ porous loofah  
387 sponge with internal microchannels as solar absorbers and water pumpers for thermal  
388 desalination. *J. Mater. Chem. A* 8, 12323-12333 (2020).
- 389 20. Y. Xu, J. Ma, Y. Han, H. Xu, Y. Wang, D. Qi, W. Wang, A simple and universal strategy to  
390 deposit Ag/polypyrrole on various substrates for enhanced interfacial solar evaporation and  
391 antibacterial activity. *Chem. Eng. J.* 384, 123379 (2020).
- 392 21. X. Y. Wang, J. Xue, C. Ma, T. He, H. Qian, B. Wang, J. Liu, Y. Lu, Anti-biofouling double-  
393 layered unidirectional scaffold for long-term solar-driven water evaporation. *J. Mater. Chem.*  
394 *A* 7, 16696-16703 (2019).
- 395 22. C. Chen, Y. Kuang, L. Hu, Challenges and opportunities for solar evaporation. *Joule* 3, 683-  
396 718 (2020).
- 397 23. V. D. Dao, N. H. Vu, S. Yun, Recent advances and challenges for solar-driven water  
398 evaporation system toward applications. *Nano Energy* 68, 104324 (2020).
- 399 24. X. J. Zha, X. Zhao, J. H. Pu, L. S. Tang, K. Ke, R. Y. Bao, L. Bai, Z. Y. Liu, M. B. Yang, W.  
400 Yang, Flexible anti-biofouling MXene/cellulose fibrous membrane for sustainable solar-  
401 driven  
402 water purification. *ACS Appl. Mater. Interfaces* 11, 36589-36597 (2019).
- 403 25. M. Kang, Z. Zhang, N. Song, M. Li, P. Sun, X. Chen, D. Wang, B. Z. Tang, Aggregation -  
404 enhanced theranostics: AIE sparkles in biomedical field. *Aggregate* 1, 80-106 (2020).
- 405 26. W. Xu, D. Wang, B. Z. Tang, *Angew. Chem. Int. Ed.* 2020, DOI: 10.1002/anie.202005899.
- 406 27. Z. Zhang, W. Xu, M. Kang, H. Wen, H. Guo, P. Zhang, L. Xi, L. Wang, D. Wang, B. Z. Tang,  
407 An all-round athlete on the track of phototheranostics: subtly regulating the balance between  
408 radiative and nonradiative decays for multimodal imaging-guided synergistic therapy. *Adv.*  
409 *Mater.* 32, 2003210 (2020).
-

- 410 28. W. Xu, M. M. S. Lee, J. J. Nie, Z. Zhang, R. T. K. Kwok, J. W. Y. Lam, F. J. Xu, D. Wang, B.  
411 Z. Tang, Three-pronged attack by homologous far-red/NIR AIEgens to achieve 1+1+1>3  
412 synergistic enhanced photodynamic therapy. *Angew. Chem. Int. Ed.* 59, 9610-9616 (2020).
- 413 29. S. Chen, J. V. John, A. McCarthy, M. A. Carlson, X. Li, J. Xie, Fast transformation of 2D  
414 nanofiber membranes into pre-molded 3D scaffolds with biomimetic and oriented porous  
415 structure for biomedical applications. *Appl. Phys. Rev.* 7, 021406 (2020).
- 416 30. G. Ni, G. Li, S. V. Boriskina, H. Li, W. Yang, T. Zhang, G. Chen, Steam generation under  
417 one  
418 sun enabled by a floating structure with thermal concentration. *Nat. Energy* 1, 16126 (2016).
- 419 31. F. Edition, Guidelines for drinking-water quality. *WHO Chron.* 38, 104–108 (2011).

420

421 **Acknowledgments:** We thank Instrumental Analysis Center of Shenzhen University for SEM  
422 analysis. **Funding:** This work was partially supported by the Natural Science Foundation for  
423 Distinguished Young Scholars of Guangdong Province (2020B1515020011), the Natural Science  
424 Foundation of China (21801169, 22005195), the Science and Technology Foundation of  
425 Shenzhen City (JCYJ20190808153415062), and China Postdoctoral Science Foundation  
426 (2020M672797). **Author contributions:** H. L., D. W., and B. Z. T. conceived and designed the  
427 experiments. W. Z. performed the synthesis AIE agent. H. L. conducted the fabrication of  
428 evaporator, solar steam generation test and collected the data. M. L., and Y. L. performed anti-  
429 bacterial experiment. H. L., W. Z., R. T. K. Kwok., J. W. Y. Lam., L. W., and D. W performed  
430 data analysis, H. L., D. W., and B. Z. T. co-wrote and revised the paper. All authors discussed the  
431 results and approved the final version of the manuscript. **Competing interests:** The authors  
432 declare that they have no competing interests. **Data and materials availability:** All data needed  
433 to evaluate the conclusions in the paper are present in the paper and/or the Supplementary  
434 Materials. Additional data related to this paper may be requested from the authors.



443

444

445

446

447

448

449

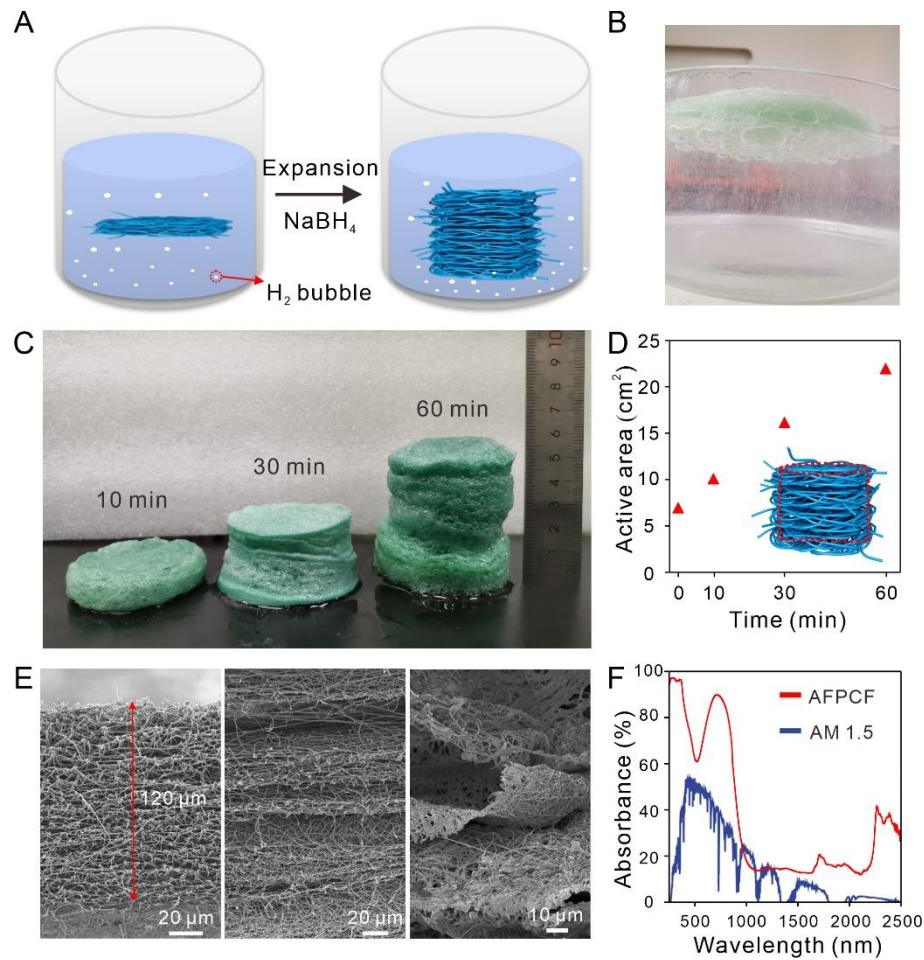
450

451

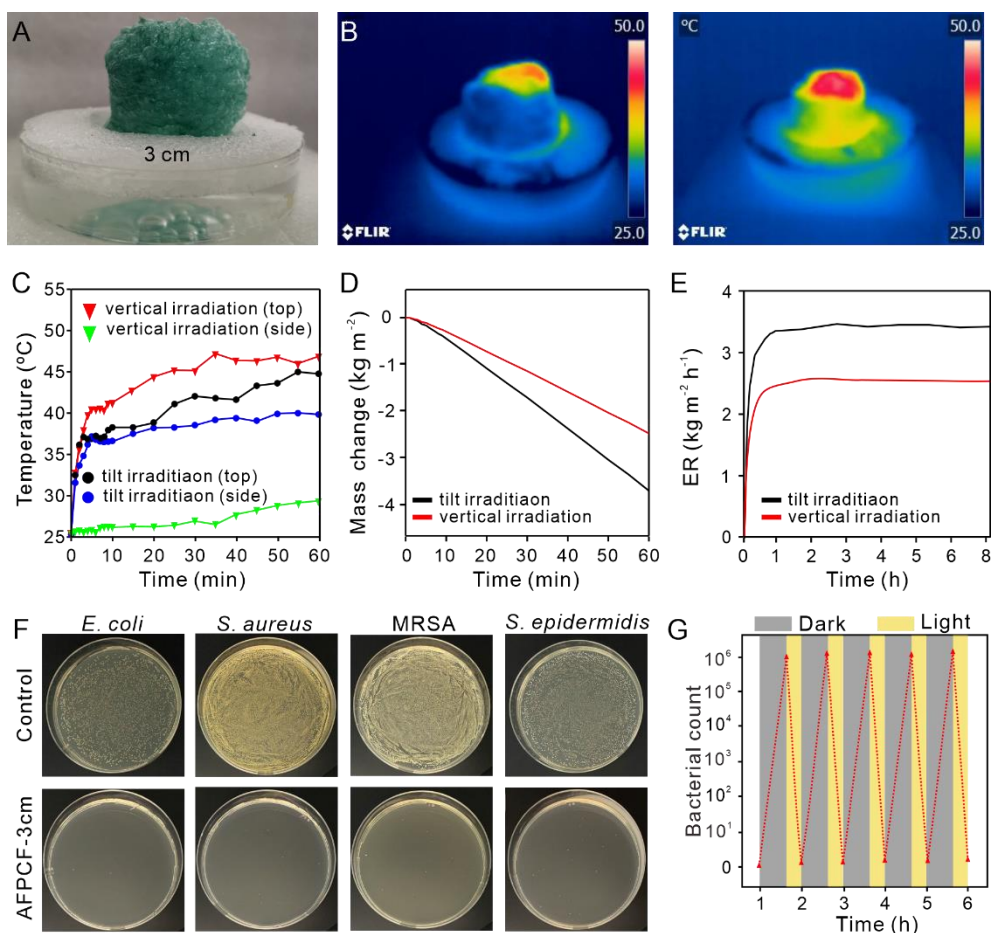
452

453

**Fig. 1. Synthesis and characterization of AIEgens.** (A) The structure of TPA-BTDH and a schematic shows the design concept of the side area-assisted evaporator. (B) The intermolecular plane distances and various intermolecular and intramolecular interactions of TPA-BTDH via Single-crystal X-ray analysis. (C) Jablonski diagram illustrating excited-state energy dissipations of TPA-BTDH. (D) Absorption and PL spectra of TPA-BTDH in THF solution. (E) ROS generation of TPA-BTDH upon xenon lamp irradiation using dichlorofluorescein (DCFH). (F) The temperature changes of TPA-BTDH powder as it was exposed to 1 sun of irradiation.



454  
 455  
 456 **Fig. 2. Fabrications and characterizations of the 3D AFPCF.** (A) Schematic illustration  
 457 of the expansion process from 2D nanofibrous mat to 3D structure. (B) A  
 458 photograph of generated bubbles as a TPA-BTDH/PMMA nanofibrous mat was  
 459 placed into 1 M  $\text{NaBH}_4$  solution. (C) Photo images of the TPA-BTDH/PMMA  
 460 nanofibrous mat after the treatment with 1 M  $\text{NaBH}_4$  solution for 10, 30 and 60  
 461 min, respectively. (D) Active area of AFPCF was calculated (surface area plus one  
 462 side area) after the treatment with 1 M  $\text{NaBH}_4$  solution for 10, 30 and 60 min,  
 463 respectively. (E) SEM images showing cross section morphologies of TPA-  
 464 BTDH/PMMA nanofibrous mat before and after the treatment of 1 M  $\text{NaBH}_4$   
 465 solution for 10 and 60 min. (F) The absorption spectra of the AFPCF ranging from  
 466 250 to 2500 nm and solar spectral irradiance weighted by standard AM 1.5G solar  
 467 spectrum.  
 468



469  
470  
471 **Fig. 3. Performance of solar-steam generation and anti-bacterial.** (A) A photo image  
472 of AFPCF with height of 3 cm enclosed by foam and floating on the water. (B) IR  
473 thermal images showing temperature changes of the AFPCF with height of 3 cm  
474 under vertical and tilted irradiation of 1 sun. (C) A comparison between the  
475 temperature rise recorded from the surface and side of AFPCF upon the vertical  
476 and tilted irradiation of the 1 sun for 60 min. (D) The mass loss of water and (E)  
477 evaporation rate of AFPCF with height of 3 cm under vertical and tilted irradiation  
478 of 1 sun for period time. (F) Photographs of *E. coli*, *S. aureus*, MRSA and *S.*  
479 *epidermidis* cultured on agar plate supplemented with TCP and AFPCF-3 cm under  
480 simulated sunlight for 10 min. (G) Five cycle antibacterial test of AFPCF under  
481 repeated simulated sunlight irradiation and dark condition. Each cycle,  $1 \times 10^6$  CFU  
482  $\text{mL}^{-1}$  *E. coli* was pipetted on the AFPCF before the dark condition.  
483



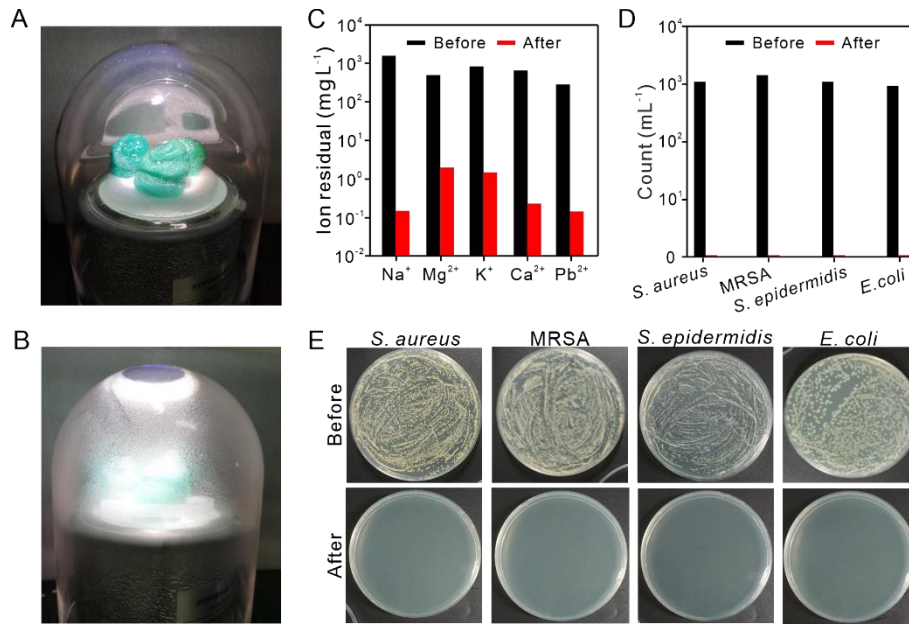


**Fig. 4. Solar water purification based on the AFPCF.** (A) A photograph of the hand-  
mand solar steam generation device containing a glass cover, a AFPCF evaporator,  
and a Dewar Flask filled with seawater or waste water. (B) A photograph showing  
clean water condensed on the inner wall of the glass cover. (C) The concentrations  
of ions (Na<sup>+</sup>, Mg<sup>2+</sup>, K<sup>+</sup>, Ca<sup>2+</sup> and Pb<sup>2+</sup>) in the simulated seawater and the collected  
clean water after evaporation. (D) The counts of bacterial clones in the simulated  
wastewater and the collected water after evaporation. (E) Photographs of *S. aureus*,  
MRSA, *S. epidermidis* and *E. coli* cultured on agar plate which are collected from  
the evaporated water.

## 497 **Supplementary Materials**

498       Supplementary material for this article is available at

499  
500       Supplementary Text

501       Figs. S1. Synthetic route to compound TPA-BTDH

502       Figs. S2. Single-crystal X-ray and calculated analysis of TPA-BTDH

503       Figs. S3. Fabrication and characterization of TPA-BTDH/PMMA nanofibrous mat.

504       Figs. S4. SEM images of TPA-BTDH/PMMA nanofibers.

505       Figs. S5. Temperature changes of the AFPCF in dry state under the irradiation of 1 sun.

506       Figs. S6. Solar steam generation performances of AFPCF.

507       Figs. S7. Temperature changes the surface of AFPCF with height of 1 cm under vertical  
508       and tilted irradiation of 1 sun.

509       Figs. S8. Anti-bacterial capacities of AFPCF under the simulated sunlight.

510       Figs. S9. Formed viable colony units of *E. coli*, *S. epidermidis*, *S. aureus* and MRSA after  
511       being treated with or without AFPCF under dark condition for 10 min, and then spread  
512       onto agar plate and incubated at 37 °C for 24 h.

513       Figs. S10. SEM images of *E. coli* and *S. aureus* after being treated AFPCF under  
514       simulated sunlight and dark condition for 10 min.

515       Figs. S11. Anti-bacterial capacities of AFPCF under the sunlight.

516       Figs. S12. Photograph showing the detailed process of the vapor condensed on the inner  
517       wall of the glass cover.

518       Figs. S13. Photograph of the collected vapor.

519       Tables S1. Crystal data and structure refinement for TPA-BTDH.

---